

Ground-based full-sky imaging polarimeter based on liquid crystal variable retarders

Ying Zhang, Huijie Zhao,* Ping Song, Shaoguang Shi, Wujian Xu, and Xiao Liang

School of Instrumentation Science & Opto-electronics Engineering, Beihang University, No. 37, Xueyuan Road, Haidian District, Beijing, 100191, China

*optoelectronicshuaa@gmail.com

Abstract: A ground-based full-sky imaging polarimeter based on liquid crystal variable retarders (LCVRs) is proposed in this paper. Our proposed method can be used to realize the rapid detection of the skylight polarization information with hemisphere field-of-view for the visual band. The characteristics of the incidence angle of light on the LCVR are investigated, based on the electrically controlled birefringence. Then, the imaging polarimeter with hemisphere field-of-view is designed. Furthermore, the polarization calibration method with the field-of-view multiplexing and piecewise linear fitting is proposed, based on the rotation symmetry of the polarimeter. The polarization calibration of the polarimeter is implemented with the hemisphere field-of-view. This imaging polarimeter is investigated by the experiment of detecting the skylight image. The consistency between the obtained experimental distribution of polarization angle with that due to Rayleigh scattering model is 90%, which confirms the effectivity of our proposed imaging polarimeter.

©2014 Optical Society of America

OCIS codes: (110.5405) Polarimetric imaging; (260.5430) Polarization; (120.5410) Polarimetry; (010.1310) Atmospheric scattering

References and links

1. K. L. Coulson, *Polarization and Intensity of Light in the Atmosphere* (A. DEEPAK Publishing, 1988).
2. A. T. Young, "Rayleigh scattering," *Phys. Today* **35**(1), 42–48 (1982).
3. H. H. Kimball, "The effect of the atmospheric turbidity of 1912 on solar radiation intensities and skylight polarization," *Bull. Mt. Weather Obs.* **5**, 295–312 (1913).
4. K. L. Coulson, "Characteristics of skylight at the zenith during twilight as indicators of atmospheric turbidity. 1: degree of polarization," *Appl. Opt.* **19**(20), 3469–3480 (1980).
5. G. Horváth, A. Barta, I. Pomozi, B. Suhai, R. Hegedüs, S. Akesson, B. Meyer-Rochow, and R. Wehner, "On the trail of Vikings with polarized skylight: experimental study of the atmospheric optical prerequisites allowing polarimetric navigation by Viking seafarers," *Philos. Trans. R. Soc. Lond. B Biol. Sci.* **366**(1565), 772–782 (2011).
6. P. Goloub, D. Tanré, J. L. Deuzé, M. Herman, A. Marchand, and F. M. Breon, "Validation of the first algorithm applied for deriving the aerosol properties over the ocean using the POLDER/ADEOS measurements," *IEEE Trans. Geosci. Rem. Sens.* **37**(3), 1586–1596 (1999).
7. J. L. Deuzé, M. Herman, P. Goloub, D. Tanré, and A. Marchand, "Characterization of aerosols over ocean from POLDER/ADEOS-1," *Geophys. Res. Lett.* **26**(10), 1421–1424 (1999).
8. J. L. Deuzé, P. Goloub, M. Herman, A. Marchand, G. Perry, S. Susana, and D. Tanré, "Estimate of the aerosol properties over the ocean with POLDER," *J. Geophys. Res.* **105**(D12), 15329–15346 (2000).
9. H. Chepfer, G. Brogniez, P. Goloub, F. M. Bréon, and P. H. Flamant, "Observations of horizontally oriented ice crystals in cirrus clouds with POLDER-1/ADEOS-1," *J. Quant. Spectrosc. Radiat. Transf.* **63**(2–6), 521–543 (1999).
10. H. Chepfer, P. Goloub, J. Spinhirne, P. H. Flamant, M. Latorato, L. Sauvage, G. Brogniez, and J. Pelon, "Cirrus Cloud Properties Derived from POLDER-1/ADEOS Polarized Radiances: First Validation Using a Ground-Based Lidar Network," *J. Appl. Meteorol.* **39**(2), 154–168 (2000).
11. H. R. Gordon and D. J. Castañó, "Coastal Zone Color Scanner atmospheric correction algorithm: multiple scattering effects," *Appl. Opt.* **26**(11), 2111–2122 (1987).
12. C. N. Adams and G. W. Kattawar, "Effect of volume-scattering function on the errors induced when polarization is neglected in radiance calculations in an atmosphere-ocean system," *Appl. Opt.* **32**(24), 4610–4617 (1993).
13. K. J. Voss and Y. Liu, "Polarized radiance distribution measurements of skylight. I. System description and

- characterization,” *Appl. Opt.* **36**(24), 6083–6094 (1997).
14. Y. Liu and K. Voss, “Polarized radiance distribution measurement of skylight. II. Experiment and data,” *Appl. Opt.* **36**(33), 8753–8764 (1997).
 15. J. Gál, G. Horváth, A. Barta, and R. Wehner, “Polarization of the moonlit clear night sky measured by full-sky imaging polarimeter at full moon: comparison of the polarization of moonlit and sunlit skies,” *J. Geophys. Res.* **106**(D19), 22647–22653 (2001).
 16. G. Horváth, A. Barta, J. Gál, B. Suhai, and O. Haiman, “Ground-based full-sky imaging polarimetry of rapidly changing skies and its use for polarimetric cloud detection,” *Appl. Opt.* **41**(3), 543–559 (2002).
 17. J. A. North and M. J. Duggin, “Stokes vector imaging of the polarized sky-dome,” *Appl. Opt.* **36**(3), 723–730 (1997).
 18. N. J. Pust and J. A. Shaw, “Dual-field imaging polarimeter using liquid crystal variable retarders,” *Appl. Opt.* **45**(22), 5470–5478 (2006).
 19. A. R. Dahlberg, N. J. Pust, and J. A. Shaw, “Effects of surface reflectance on skylight polarization measurements at the Mauna Loa Observatory,” *Opt. Express* **19**(17), 16008–16021 (2011).
 20. N. J. Pust, A. R. Dahlberg, M. J. Thomas, and J. A. Shaw, “Comparison of full-sky polarization and radiance observations to radiative transfer simulations which employ AERONET products,” *Opt. Express* **19**(19), 18602–18613 (2011).
 21. Y. Zhang, H. J. Zhao, and N. Li, “Polarization calibration with large apertures in full field of view for a full Stokes imaging polarimeter based on liquid-crystal variable retarders,” *Appl. Opt.* **52**(6), 1284–1292 (2013).
 22. D. S. Sabatke, M. R. Descour, E. L. Dereniak, W. C. Sweatt, S. A. Kemme, and G. S. Phipps, “Optimization of retardance for a complete Stokes polarimeter,” *Opt. Lett.* **25**(11), 802–804 (2000).
 23. J. S. Tyo, “Noise equalization in Stokes parameter images obtained by use of variable-retardance polarimeters,” *Opt. Lett.* **25**(16), 1198–1200 (2000).
 24. J. S. Tyo, “Design of optimal polarimeters: maximization of signal-to-noise ratio and minimization of systematic error,” *Appl. Opt.* **41**(4), 619–630 (2002).
 25. B. Suhai and G. Horváth, “How well does the Rayleigh model describe the E-vector distribution of skylight in clear and cloudy conditions? A full-sky polarimetric study,” *J. Opt. Soc. Am. A* **21**(9), 1669–1676 (2004).

1. Introduction

For a long time, scientists in different countries are devoted to the research of skylight. In early stages, explaining the phenomenon of skylight, such as the color of the sky, and rainbow and so on has been focused on one of scientists’ researches [1,2]. Since the polarization of the skylight was firstly investigated by Arago in 1809, the researches on the characters of the polarization of skylight have been implemented widely. The skylight is polarized due to the scattering from the air molecule in atmosphere and aerosol particles before arriving at the ground, and distribution of the polarization state of the skylight can be described by some rules [3]. Many researches show that the precise navigation even can be realized by analyzing the polarization state distribution of skylight in different cases of weather and different solar elevation angles [4]. Gáboret et al. found that the navigators during 750 to 1050 AD could identify the direction in Atlantic using the polarized light [5]. In addition, the polarization detection method can be utilized to obtain important information for aerosol particle and the pollution particle in atmosphere [6–8].

What is more, the polarization detection of the skylight can also be used to analyze the internal physical feature of the cloudiness, such as whether there are cirrus clouds, the advantage direction in ice crystals and the size and the distribution of the aerosol particles [9, 10]. Detection of the intensity and polarization state of skylight is also important in atmospheric correction of remotely sensed data [11]. It has been improved that neglecting the polarization in radiance calculations in an atmosphere–ocean system could introduce the errors as large as 30% [12].

Currently, the ground imaging polarimeters have been used widely in detecting skylight. Voss and Liu proposed the RADS-II system based on the fish-eye lens and polarizer [13,14]. The imaging polarization detection of the skylight is realized by rotating the polarizer with the precision of 2% for linear polarization during the measurement period of 1.5~2 min. Gal and Pomozi presented a full-sky imaging polarimeter with simple operation and convenience of installation [15]. The main deices are mounted on a tripod, with a 180° fish-lens roll-film photographic camera. The time for a measurement is about 6~8 s.

In conclusion, the imaging polarimeters described above are all based on single polarizer, which is only capable to detect the linear polarization light. In addition, it is necessary to utilize mechanical rotating to realize the modulation of polarization state of input light. So, the strict consistency between the camera and rotating is required, which results in the low precision of polarization state modulation, small frame rate, low reliability and large volume.

Rapid polarization imaging for a single wavelength is a driving requirement to accurately capture clouds in motion [16]. Horvath et al. designed a full-sky imaging polarimeter with three lenses and three cameras. Three cameras are operated for pointing to the zenith, and every camera is equipped with a fish-eye lens and a polarizer with 0° , 60° , and 120° , respectively. North, Dugginet et al. utilized four lenses and four cameras to obtain the partial *STOKES* vectors and the derived images [17]. Their proposed imaging polarimeter can obtain the four images of the linear polarization intensities with four polarization directions in the same time by controlling the synchronously of four CCD cameras.

However, the optical path and configuration of this multi-camera and multi-path polarimeter imaging system are comparatively complicated, so, the volume and weight are still large. Then, Nathan and Joseph designed a dual field-of-view imaging polarimeter [18]. Their proposed imaging polarimeter is based on LCVR, so, the polarization state can be changed rapidly. Generally, it takes only 0.4 s to obtain the full-polarization images for a wavelength. As a result, the errors due to the environmental fluctuation such as the displacement caused by wind, and the movement of the clouds, can be eliminated. In addition, the influences of different weathers on the polarization distribution of the skylight can be investigated by this imaging polarimeter in the cases of different weather. Polarization calibration is executed point by point for all of the imaging pixels. However, the influences of incidence angle of light on the LCVR are not analyzed and the polarization calibration method is complicated for the 180° field-of-view polarimeter [19, 20].

In this paper, we propose and investigate an overall design of a ground-based full-sky imaging polarimeter based on LCVRs. What is more, the corresponding polarization calibration for our proposed imaging polarimeter is presented, with the field-of-view multiplexing and piecewise linear fitting. By experimental investigation, it is found that this imaging polarimeter is useful to detect the whole polarization of skylight, with fast response, high precision, broad wavelength range, high transmittance, low volume and power, and light weight.

2. Principle

2.1 Polarization detection based on the Stokes vectors

The intensity and the polarization states of light wave can be described by Stokes vectors composed of four parameters, where the light could be monochromatic, non-monochromatic, full polarized, partially polarized or natural light. The four Stokes parameters are the time average of the light intensity, which can be measured directly. Therefore, the Stokes vectors are often used in polarization detection, defined as follows:

$$S = \begin{pmatrix} I \\ Q \\ U \\ V \end{pmatrix} = \begin{pmatrix} \langle E_x^2(t) \rangle + \langle E_y^2(t) \rangle \\ \langle E_x^2(t) \rangle - \langle E_y^2(t) \rangle \\ 2 \langle E_x^2(t) \rangle \langle E_y^2(t) \rangle \cos(\delta_y(t) - \delta_x(t)) \\ 2 \langle E_x^2(t) \rangle \langle E_y^2(t) \rangle \sin(\delta_y(t) - \delta_x(t)) \end{pmatrix} = \begin{pmatrix} I_{0^\circ} + I_{90^\circ} \\ I_{0^\circ} - I_{90^\circ} \\ I_{45^\circ} - I_{135^\circ} \\ I_R - I_L \end{pmatrix} \quad (1)$$

where, $E_x(t)$, $E_y(t)$, $\delta_x(t)$, $\delta_y(t)$ are the amplitudes and the phases of the electric field in x and y direction. $\langle \sim \rangle$ indicates figuring out the time average of the electric field intensity. I_{0° , I_{90° , I_{45° , and I_{135° indicate the intensity of the light passing through a polarizer with 0° , 90° , 45° , -45° , respectively. I_R and I_L are the intensity of light with left-handed and right-handed polarization.

Then, the degree of linear polarization (DOLP) can be expressed as:

$$DOLP = \frac{\sqrt{Q^2 + U^2}}{I} \quad (2)$$

Analogously, the degree of circular polarization (DOCP) can be defined as:

$$DOCP = \frac{|V|}{I} \quad (3)$$

The degree of polarization (DOP) is

$$DOP = \frac{\sqrt{Q^2 + U^2 + V^2}}{I} \quad (4)$$

The azimuth angle of polarization (AOP) is

$$AOP = \frac{1}{2} \arctan \frac{Q}{U} \quad (5)$$

When the light passes through a device, the Stoke vector (S_{out}) of the output light is the product of the Mueller matrix of the device (M) and input Stokes vector (S_{in}):

$$S_{out} = M \times S_{in} \quad (6)$$

The Mueller matrix of N series devices can be obtained by:

$$M_{comb} = M_N M_{N-1} \dots M_2 M_1 \quad (7)$$

For a polarization measurement system, there are usually a phase retarder and a linear polarimeter. So, by calculating the Stokes vector of the light reflected by the object, we can obtain the state of surface, physical and chemical properties of the object, which is the theoretical basis of polarization remote sensing.

2.2 Rayleigh scattering model

The distribution of intensity and polarization of the skylight can be described by the Rayleigh scattering by molecules in the atmosphere [1]. As shown in Fig. 1, the reference plane can be defined by the incident and scattered light. Then, the incident natural light can be decomposed into two orthogonal linear polarized components, E_r^o and E_l^o , which are of the same intensity. When the scattering angle θ is not 0° , or 180° , the intensity of the vertical component E_r^s is more than that of the horizontal component E_l^s . The polarization direction is determined by the component with the larger intensity, therefore, the law of the Rayleigh scattering can be concluded as that, after the natural light occurs the Rayleigh scattering, the polarization direction of the scattered light is perpendicular to the scattering plane defined by the incidence light and the scattered light. The DOP can be described as the following equation:

$$DOP(\theta) = \frac{1 - \cos^2 \theta}{1 + \cos^2 \theta} DOP_{max} \quad (8)$$

where DOP_{max} is the maximal DOP.

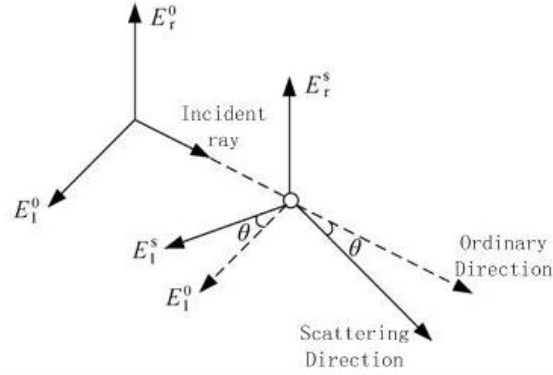


Fig. 1. Schematic of Rayleigh scattering model.

The distribution of DOP and the polarization azimuth of the skylight can also be described by Rayleigh scattering model. Therefore, we can take a position on the ground as the observation point. The polarization information of the E vector in horizontal coordinate system for a point P in sky is shown in Fig. 2, where S is the sun, and Z is the zenith. Due to the Rayleigh scattering theory, the measured polarization of skylight is perpendicular to the plane, which is composed of the sun S , observation point O on the ground, and the observation point P in the sky. The polarization angle φ can be defined as the angle between the polarization direction of P and the meridian plane ZPO through P . The polarization of E vector of point P is perpendicular to the plane OPS . So, the polarization azimuth $\varphi = 90^\circ - \angle ZPS$. For the spherical triangle ZPS , it can be obtained by the *Cosine* law:

$$\cos \theta = \sin(h_p) \sin(h_s) + \cos(h_p) \cos(h_s) \cos(A_s - A_p) \quad (9)$$

where the scattering angle θ is the angle between OS and OP , h_s and h_p are the altitude angles of the sun S and point P , A_s and A_p are the azimuths of the sun S and the P point. Here the azimuth of South is set to be 0° , so, the azimuth of west is 90° . Then, according to the *Sine* law, we can get:

$$\frac{\sin(\angle ZPS)}{\sin(90^\circ - h_s)} = \frac{\sin(|A_s - A_p|)}{\sin \theta} \quad (10)$$

Therefore, it can be obtained:

$$\cos \varphi = \frac{\sin(|A_s - A_p|)}{\sin \theta} \cos(h_s) \quad (11)$$

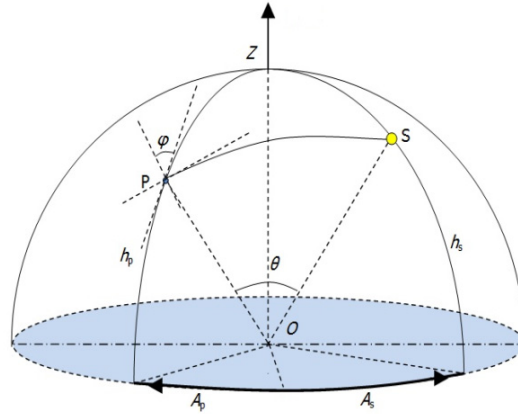


Fig. 2. The polarization of E vector of P point in the sky.

We can accurately calculate the positions of the sun and the moon in the horizontal coordinate system and describe the polarization distribution of the skylight combining the Rayleigh scattering theory when the geographical location and the time are known. Therefore, the precision of our proposed LCVR based imaging polarimeter can be evaluated by comparing the detection results to that by Rayleigh scattering theory.

3. The imaging polarimeter

3.1 The characteristic of incident angle of LCVR

The polarization detection theory of our ground-based full-sky imaging polarimeter based on LCVRs is same as the system we designed before [21]. For our proposed imaging polarimeter, the full polarization detection is realized by two LCVRs and the polarizers behind them. LCVR is used as a device with tunable phase delay that can be modulated by the voltage. This voltage is set to be four different values and there can be four different phase delay. Then, four intensity images due to four different phase delay can be obtained. So, there is a linear equation group. We can calculate the four components of the Stokes vector, S_0 , S_1 , S_2 , and S_3 by matrix, and the full polarization vectors of the incident light are achieved. The precision of polarization detecting of incident light is determined by the phase delay of the LCVR, so, it is necessary to investigate the relationship between the phase delay and the incident angle of the light.

The geometric model for the incident angle of light and the molecule axis of the liquid crystal is shown in Fig. 3. The incident light arrives at the surface of LCVR with an incident angle. An x - y - z coordinate system can be established with the incident point as the origin and the incident surface of LCVR as the x - y plane. Here Φ is the angle between z axis and the incident light in x - y plane, ξ is the angle between z axis and the refracted light in x - z plane, β is the angle between the molecule axis and x - y plane, s is the angle between x axis and the projection of molecule axis in x - y plane, α is the angle between the molecule axis and the refracted light, and n is the refractive index of the liquid crystal.

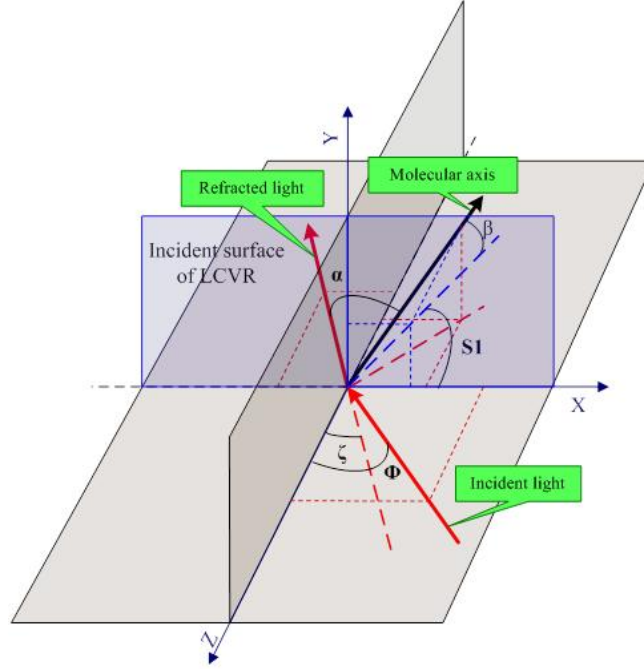


Fig. 3. The geometric model for the incident angle of light and the molecule axis of the liquid crystal.

According to the geometric model in Fig. 3, we can get:

$$\cos \alpha = \sin \xi \cos \beta \cos(s) - \cos \xi \sin \beta \quad (12)$$

$$\xi = \arcsin(\sin \Phi / n) \quad (13)$$

The phase delay δ of LCVR is a function of the incident angle Φ , and is also a function of tilt angle α of the molecule axis:

$$\delta = \frac{B_0 t (1 - \sin^2 \alpha)}{\lambda \cos \xi} \quad (14)$$

where B_0 is the birefringence of liquid crystal with a zero voltage, t is the thickness of the liquid crystal, and λ is the wavelength of light.

When the incident wavelength is 530 nm, scattering angle $\theta_0 = 45^\circ$, the relationship between phase delay of LCVR and applied voltage in the cases of different incident angles is calculated by Matlab, and shown in Fig. 4.

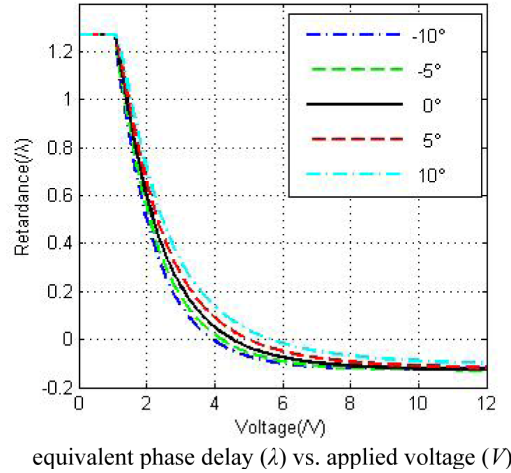


Fig. 4. The relationship between phase delay of LCVR and applied voltage in the cases of different incident angles.

Then, from Fig. 4, it can be found that:

1. When the applied voltage exceeds a threshold (~ 1 V), phase delay decreases observably with the increase of applied voltage, when applied voltage is in the range between 1~6 V. It means that LCVR is with advantages of low tuning voltage, easy to control, and continuingly adjustable.
2. When the applied voltage exceeds 6 V, the curve between the phase delay and applied voltage tunes to be flat, which results from the balance between torques due to the liquid crystal molecule and the external electric field.
3. When the applied voltage is constant, the phase delay of LCVR increases with the increase of the incidence angle ($0^\circ \sim 10^\circ$), and decreases with the decrease of the incidence angle ($-10^\circ \sim 0^\circ$).

In the cases of different incident angles, the Mueller matrix of the imaging polarimeter is changed due to the difference between the phase delay of LCVR and the fast axis angle. As a result, the condition numbers are changed, too. The quantization error and Stokes error can be determined by condition numbers [22–24], so, in order to improve the precision of polarization detection, the incident angle of the LCVR need to be limited.

Then, Mueller matrix of the full polarization detection system with two LCVRs can be expressed as follows:

$$M_{PMC} = M_{LP} \times M_{LCVR2} \times M_{LCVR1} \quad (15)$$

When applied voltage is constant, M_{PMC} is a function of the incidence angle Φ . Accordingly, the circumference average condition numbers can be described by the following equation:

$$Cond_{ave}(\Phi) = \|M_{PMC}(\Phi)\|_2^* \|M_{PMC}(\Phi)^{-1}\|_2 \quad (16)$$

where $\|M_{PMC}(\Phi)\|_2$ is the spectral norm of $M(\Phi)$, and $\|M_{PMC}(\Phi)^{-1}\|_2$ is the spectral norm of $M(\Phi)^{-1}$.

Then, $cond_{ave}$, the circumference average of the Mueller matrix condition numbers for the full polarization detection system, when the incidence angle Φ changes from 0° to 8° , is shown in Table 1, which is calculated by Matlab. According to Table 1, $cond_{ave}$ reaches the minimum when the incident angle is 0° , and the precision of the full polarization detection

reaches the maximum. The value of $cond_{ave}$ increases with the increase of Φ . To assure the detection precision, the difference between the maximum and the minimum of $cond_{ave}$ should be less than 0.5. As a result, it is required to control the maximum of incident angle on LCVR to be less than 5° .

Table 1. Circumference Average of the Mueller matrix condition numbers in full polarization detection components

$\Phi(^{\circ})$	0	1	2	3	4	5	6	7	8
$cond_{ave}$	1.74	1.80	1.87	1.96	2.08	2.21	2.38	2.58	2.84

3.2 Design of imaging polarimeter

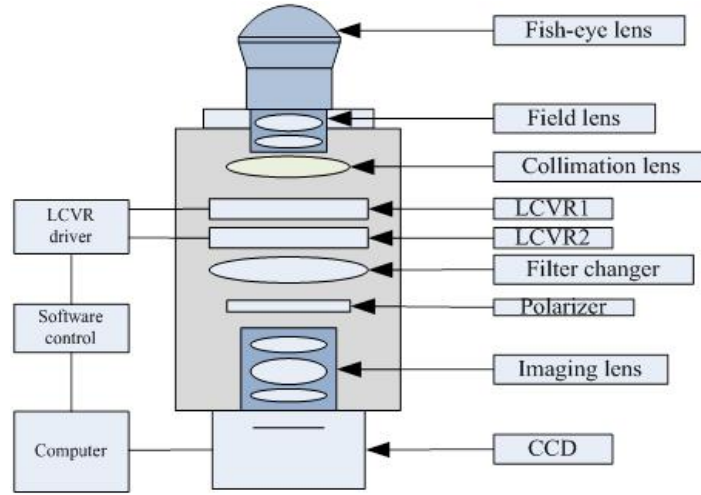


Fig. 5 Schematic of the proposed imaging polarimeter.

Our proposed LCVR based imaging polarimeter is composed of a set of pre-lenses, two LCVRs (*Meadowlark LRC-200*), a polarizer (*Meadowlark DP-100-VIS*), a filter (*China Daheng Group, GCC-2020*), a set of post-imaging lenses and a CCD camera (*Qimaging Exi-1394*), which is shown in Fig. 5. The pre-lenses consist of a fish-eye lens, a field lens and a collimating lens. The skylight passes through the pre-lenses with hemisphere field of view and an image is formed at its focal plane, and then passes through the two LCVRs, a filter, a polarizer, and an imaging lens. At last, the second image is detected by a CCD camera. The image from CCD camera is collected and transmitted, and stored in a computer to keep perform the processing. Compared to the system with the small field of view full polarization multi-wavelength imaging designed before, the structure of our proposed imaging polarimeter is quite different. The design of this imaging polarimeter is based on the analysis on the characteristics of incident angle of the LCVR. The field angle of the fish-eye lens can reach a hemisphere field-of-view of 180° . The angle of the light passing through the fish-eye lens is adjusted by the field lens and collimating lens. So, the incident angle of light on the LCVR is within $\pm 4.7^\circ$, which the accuracy of the polarization modulation on incident light can be ensured.

4. Polarization calibration

The instrument matrix of the system needs to be calibrated by polarization calibration.

The quantitative relationship between the output signals from every units of the imaging polarimeter and the polarization information of its corresponding actual object can be obtained during the process of the polarization calibration. So, the response degree equation for every imaging unit and the instrument matrix can be obtained. In the case of that the

wavelength of the incident light and the polarization state (S_{IN}) are constant, four different phase delay of two LCVRs can be realized by applying four different voltages. Then, the intensity for the four images (I_{0-3}) can be obtained.

The instrument matrix can be expressed as:

$$M_{INS} = \begin{pmatrix} a_{00} & a_{01} & a_{02} & a_{03} \\ a_{10} & a_{11} & a_{12} & a_{13} \\ a_{20} & a_{21} & a_{22} & a_{23} \\ a_{30} & a_{31} & a_{32} & a_{33} \end{pmatrix} \quad (17)$$

There is a relationship as:

$$I_{OUT} = \begin{pmatrix} I_0 \\ I_1 \\ I_2 \\ I_3 \end{pmatrix} = M_{INS} \times S_{IN} \quad (18)$$

Four types of linear polarized light and two types of circularly polarized light can be generated by a polarized light source. Every polarization state is repeated for five times. The images are collected and the light intensities detected by the CCD can be obtained. Then, the Stroke parameters matrix, light intensity matrix and covariance matrix can be obtained. Finally, the instrument matrix can be calculated by the least squares method with unequal precision [21].

Current polarization calibration method is used in the case of that the angle of field-of-view is in the range of $\pm 10^\circ$. However, in this paper, the angle is $\pm 90^\circ$ in our proposed imaging polarimeter. Furthermore, conventional polarized light source is not able to cover the entire field-of-view. Due to the axisymmetric of the optical structure of the imaging polarimeter, the instrument matrix of every pixel of CCD is all symmetrical at O . In other words, the instrument matrix of each pixel of CCD is equivalent due to that all pixels have the same distance from O . So, theoretically, only the instrument matrix of pixels on one arbitrary diameter OR of the CCD is needed to be calibrated, then, all instrument matrixes of the pixels can be calculated for the entire CCD. Based on this principle, we proposes a method of polarization calibration by the field-of-view multiplexing and piecewise linear fitting, which is shown in Fig. 6.

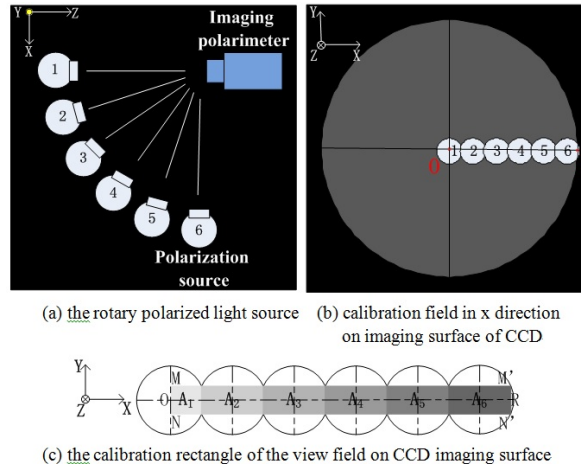


Fig. 6. polarization calibration in full field-of-view.

First of all, the optical axis of polarized light source is aligned to that of the imaging polarimeter, as shown in Fig. 6(a). By the means of this calibration process in that position, the polarization calibration can be achieved for every pixel in the rectangular A_1 , which is in $0\sim 8^\circ$ field-of-view along the x axis on the CCD surface, as shown in Fig. 6(b). Then, the vertex of the first lens in the calibration system is considered as the centre of the circle, and a circle can be obtained with the radius of distance between the circle centre and the centre of the light source. Then, the light source is turned 18° to position 2 in x - z plane, as shown in Fig. 6(a). The overlap field-of-view angle before and after the rotation is 2° . Next, the polarization calibration for the pixels in the rectangular A_2 within the $8^\circ \sim 24^\circ$ of field-of-view can be implemented, as shown in Fig. 6(b). By continuing rotating the light source, the polarization calibration for all pixels in a specified 16° field-of-view can be finished by every rotation. After rotating the light source for 5 times, the polarization calibration for all pixels in the rectangular of view field in $0^\circ \sim +90^\circ$ can be completed, as shown in Fig. 6(c). The length of the rectangular $MNN'M'$ composed by rectangular A_1 to A_6 is 351 pixels in size, which equals to the radius of CCD imaging surface. The instrument matrix of an arbitrary pixel in the rectangle can be calculated by:

$$M_{INS(i,j)} = \begin{pmatrix} (a_{00})_{(i,j)} & (a_{01})_{(i,j)} & (a_{02})_{(i,j)} & (a_{03})_{(i,j)} \\ (a_{10})_{(i,j)} & (a_{11})_{(i,j)} & (a_{12})_{(i,j)} & (a_{13})_{(i,j)} \\ (a_{20})_{(i,j)} & (a_{21})_{(i,j)} & (a_{22})_{(i,j)} & (a_{23})_{(i,j)} \\ (a_{30})_{(i,j)} & (a_{31})_{(i,j)} & (a_{32})_{(i,j)} & (a_{33})_{(i,j)} \end{pmatrix} \quad (19)$$

where i stands for the line number of the pixel and j is the row number, i and j are integers with $-3 \leq i \leq 3$, $0 \leq j \leq 350$. When $i = 0$, $M_{INS(0,j)}$ is the instrument matrix for all pixels on the radius OR of the imaging surfaces. For an arbitrary pixel N in the CCD imaging surface full field-of-view, the instrument matrix can be calculated using the step by step linear fitting. Assume that there is n pixels in the distance between pixel N and the centre O of the imaging surface, rounding n into an integer between $[n]$ and $[n + 1]$, by linear fitting, we can get:

$$\frac{M_{INS(x_N, y_N)} - M_{INS(0, [n])}}{n - [n]} = \frac{M_{INS(0, [n+1])} - M_{INS(0, [n])}}{1} \quad (20)$$

namely,

$$M_{INS(x_N, y_N)} = (M_{INS(0, [n+1])} - M_{INS(0, [n])})(n - [n]) + M_{INS(0, [n])} \quad (21)$$

where $M_{INS(x_N, y_N)}$ is the instrument matrix of pixel N . $M_{INS(0, [n])}$ and $M_{INS(0, [n+1])}$ are the instrument matrices of the pixels with the distance of $[n]$ and $[n + 1]$ from x axis to the centre O , respectively.

The errors of the instrument matrixes of partial pixels on the direction of the radius OR is induced by the systematic and operation errors during the calibration. The error in field-of-view of arbitrary pixels and its neighbor pixels on y direction is between 0° and 0.257° . Due to such a small field-of-view difference, the difference between the instrument matrixes can be considered to be a small item. In order to improve the calibration precision, the average of the instrument matrix and that of its neighbor two pixels on y direction is calculated to get a new instrument matrix as the corrected calibration instrument matrix:

$$\overline{M}_{INS(0,j)} = \frac{M_{INS(-1,j)} + M_{INS(0,j)} + M_{INS(1,j)}}{3} \quad (22)$$

Then, for an arbitrary pixel N in the field-of-view, the instrument matrix can be calculated by:

$$\overline{M}_{INS(x_N, y_N)} = (\overline{M}_{INS(0, [n+1])} - \overline{M}_{INS(0, [n])})(n - [n]) + \overline{M}_{INS(0, [n])} \quad (23)$$

5. Experimental results and discussion

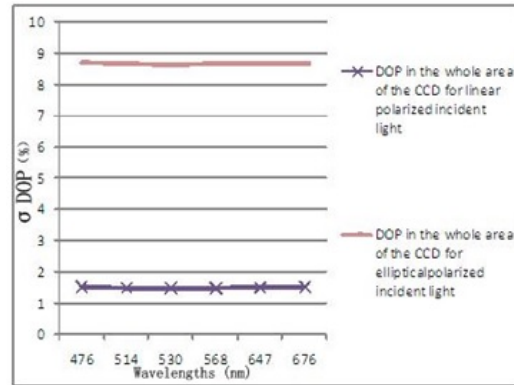
5.1 Standard deviation for the proposed polarization calibration

In order to evaluate the feasibility and performances of the ground-based full-sky imaging polarimeter based on LCVRs, the experiments for standard deviation (STDV) measurement for proposed polarization calibration and performances of imaging polarimeter using proposed polarization calibration are executed.

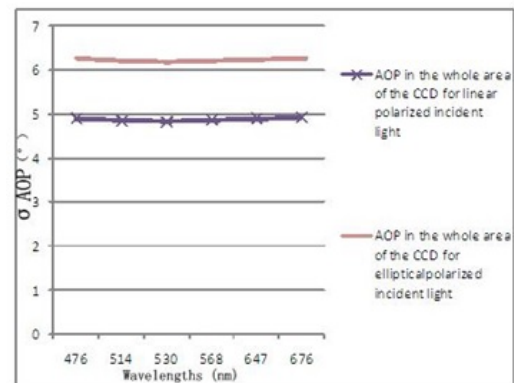
Table 2. Experimental results for STDV of the polarization calibration ($\lambda = 476$ nm)

Polarized state of incident light	Instrument matrix	STDV in whole area of CCD			
		σ_{DOLP}	σ_{DOCP}	σ_{DOP}	σ_{AOP}
Linear polarized light generated by a 30° linear polarizer	$M_{INS(x_N, y_N)}$	1.61%	0.68%	1.74%	6.12°
	$\overline{M}_{INS(x_N, y_N)}$	1.43%	0.53%	1.52%	4.91°
Elliptical polarized light generated by a 30° linear polarizer and a quarter waveplate	$M_{INS(x_N, y_N)}$	7.62%	4.62%	8.92%	7.23°
	$\overline{M}_{INS(x_N, y_N)}$	7.46%	4.51%	8.71%	6.28°

It is worth noting that the STDV of DOP and AOP are used to describe the performances of the proposed polarization calibration here. Then, the STDV of the polarization calibration for two types of polarized light with $\lambda = 476$ nm is executed and shown in Table 2, where $M_{INS(x_N, y_N)}$ and $\overline{M}_{INS(x_N, y_N)}$ are used as the calibrated instrument matrix, respectively. What is more, the STDV of DOP and AOP in six different wavelength bands are shown in Fig. 7. It is found that in the case of $M_{INS(x_N, y_N)}$ being used as the calibrated instrument matrix, the STDV of DOP and AOP are 1.74% and 6.12° for linear polarized light, 8.92% and 7.23° for elliptical one in the whole area of the CCD, respectively. In the other case of $\overline{M}_{INS(x_N, y_N)}$ being used as the calibrated instrument matrix, the STDV of DOP and AOP are decreased to 1.52% and 4.91° for linear polarized light, 8.71% and 6.28° for elliptical one, respectively. It is proved that our proposed method of polarization calibration is effectively, especially for $\overline{M}_{INS(x_N, y_N)}$ used as the calibrated instrument matrix.



(A)



(B)

Fig. 7. The STDV of DOP (A) and AOP (B) by different wavelengths.

It can be also seen that the STDV of DOP and AOP in the five bands for linear polarized light are nearly equal, while different for elliptical ones. This is because the polarization state of the incident elliptical light generated by a linear polarizer and a quarter waveplate is different for different bands. The value of the quarter waveplate is dependent upon the incidence angle of light and the wavelength, and the exact position of the fast axis changes with wavelength.

5.2 Performances of the proposed imaging polarimeter based on LCVRs

Our proposed imaging polarimeter is equipped on a tripod with compass, level and 180° rotating platform, on top of the our university stadium (coordinates: E116.3456 N39.9795), as shown in Fig. 8.

The polarization angle images by experimental and Rayleigh model are shown in Fig. 9. The experimental polarization angle images are obtained by the daylight from 35° zenith angle area, during 7~10 AM, with different solar altitude angles, and the same wavelength (476 nm). The theoretical polarization angle images calculated by Rayleigh model are also presented for comparison. Due to the instrument error during experiment, there is a small deviation between experimental and theoretical results. It is found that the experimentally measured polarization angles of daylight with a difference within 5° from the theoretical results can be considered as similar points [25]. The similarity of the imaging polarimeter can be defined as the ratio of amount of similar points to that of difference. In the cases of different solar altitude angles, the similarity of our experimental polarization angles is better

than 90% to Rayleigh model. Even when the solar altitude angle is 55° , there is a 97% similarity. This proves the feasibility of our imaging polarimeter and the calibration. It is also found that with the change of the solar altitude angle, the daylight polarization angle distribution is changing. In particular, in the area close to the sun, the polarization angle distribution is varied dramatically, whereas in the area far away from the sun there is a relatively smooth change in polarization angle.



Fig. 8. Implement of experiment.

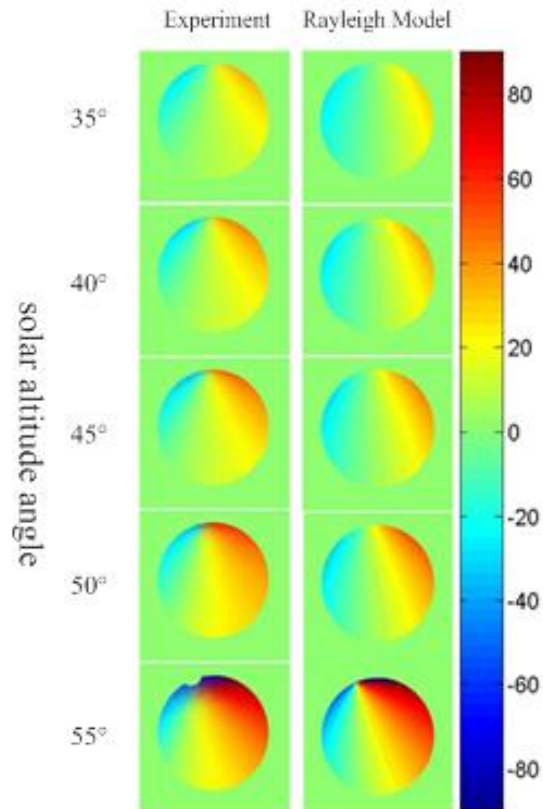


Fig. 9. The polarization angle images by experimental and Rayleigh model.

The experimental DOP and AOP in different wavelengths with the solar altitude angle of 35.8° are shown in Fig. 10. It is found that for the same solar altitude angle, and different wavelengths, the polarization angle distribution of skylight is basically the same, which obeys the distribution calculated by Rayleigh model. However, DOP decreases with the increase of wavelength, which is mainly due to that the atmospheric particles' scattering intensity of skylight is weakened with the increase of wavelength. For the experimental results, the lowest, and the highest DOP can be obtained in the area near sun and in the case of that the solar altitude angle is 90° . That is also consistent with the calculating results by the Rayleigh model.

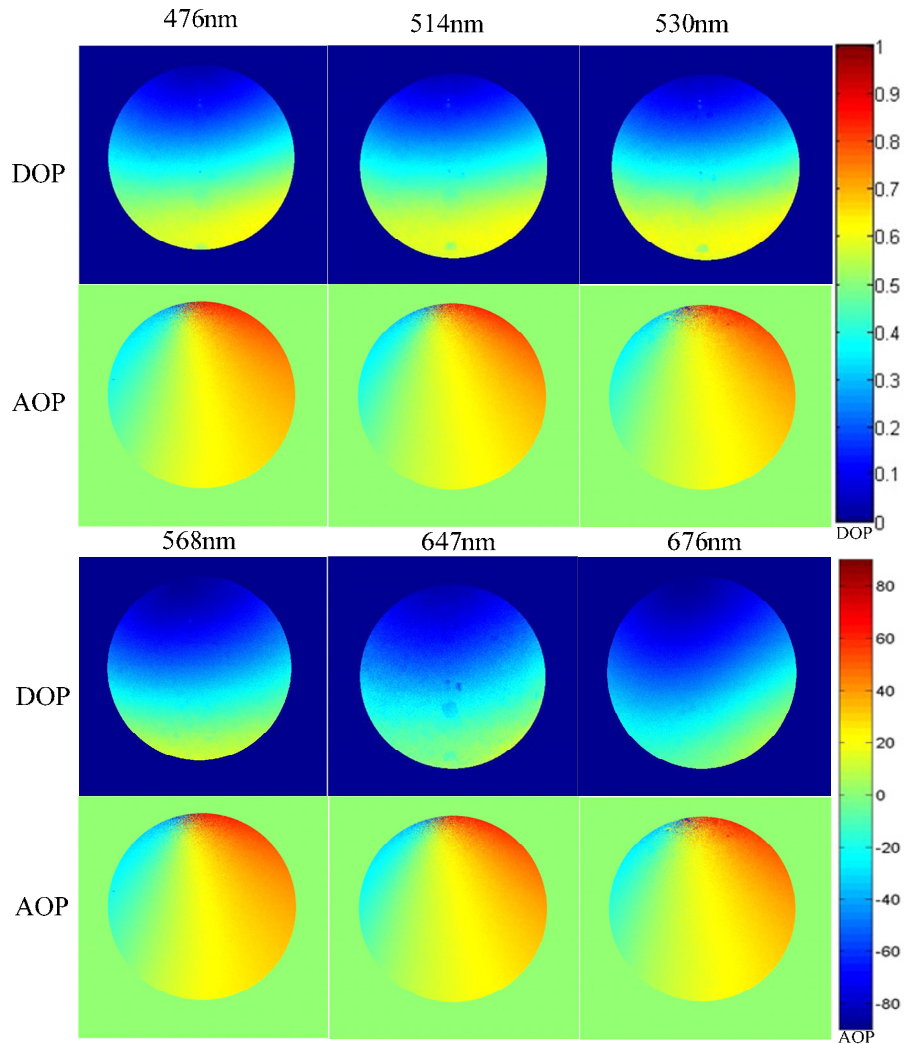


Fig. 10. Experimental DOP and AOP in different wavelengths with the solar altitude angle of 35.8° .

6. Conclusions

A ground-based full-sky imaging polarimeter using LCVRs is proposed in this paper. First of all, the characteristics of the incident angle of LCVR are studied based on the electronically controlled birefringence characteristics of LCVR. Then, the design of the hemisphere field-of-view imaging polarimeter structure is achieved. In order to ensure the accuracy of

polarization detection, the incident angle of the LCVR is modulated by the field lens and collimating lens. In addition, based on the rotational symmetry feature of the imaging polarimeter, the field-of-view multiplexing and piecewise linear fitting are proposed and the polarization calibration for hemisphere field-of-view is realized. The STDV of DOP and AOP are 1.52% and 4.91 ° for linear polarized light, and 8.71% and 6.28 ° for elliptical one in the whole area of the CCD, respectively. Finally, the polarization angle images of daylight are obtained in experiment, and the similarity of our experimental polarization angles is better than 90% to Rayleigh model.

The daylight polarization angular distribution alters with the change of the solar altitude angle. With the same solar altitude angle, and different wavelengths of daylight, the polarization angle has basically the same distribution, and DOP decreases with the increasing of wavelength. All the experimental results obey distribution by the Rayleigh model. These conclusions are useful in navigation technology, which is one of the most applicable values of the daylight polarization characteristics.

Acknowledgments

This work was supported by the National Natural Science Foundation of China (No. 61107013) and the National Natural Science Foundation of China (No. 61227806).